SUPPORTING INFORMATION

Descriptor-guided Design and Experimental Synthesis of Metal-doped TiO_2 for Propane Dehydrogenation

Liqi Xiao[a], Zean Xie[b], Shaojia Song[a], Zhiping Zhao[a], Ming Ke[a], Weiyu Song[a,*], Jian Liu[a,*], Zhen Zhao[a,b,*]

[a]State Key Laboratory of Heavy Oil Processing, China University of Petroleum Beijing 102249, P.R. China

[b]Institute of Catalysis for Energy and Environment, Shenyang Normal University, Shenyang 110034, China

Corresponding author: songwy@cup.edu.cn, liujian@cup.edu.cn, zhenzhao@cup.edu.cn

1. Derivation of Microkinetic Equation Model

Differential equation models are used to study each elementary reaction, and thus the entire propane dehydrogenation reaction. The reaction rate constant of the elementary reaction can be expressed by the Eyring equation:

$$k=Ae^{\frac{E_a}{k_bT}} \quad (1)$$

$$A=\frac{k_bT}{h}\frac{Q^{TS}}{Q} \quad (2)$$

Where, k is the reaction rate constant. A is the pre-factor. k_b is the Boltzmann constant. T is temperature. h is the Planck constant. E_a is the energy barrier of the elementary reaction. Q and Q^{TS} are partition functions of ground state and transition state.

In the elementary reaction, the entropy change can be ignored, and the pre-finger factor can be approximated. During the adsorption process, $E_a = 0$, the entropy change can be expressed by a partition function, that is, the product of the translation, rotation, and vibration partition functions corresponding to the configurational degrees of freedom of the surface complexes.

In the transition state, there are two degrees of freedom in translation, three degrees of freedom in rotation, and 3N-5 degrees of freedom in vibration. In the initial state, all gas molecules in the gas phase are considered to be included.

Based on the above assumptions, the adsorption reaction rate equation:

$$k_{ads}=\frac{PA}{\sqrt{2\pi mk_bT}}S \quad (3)$$

where P is the partial pressure of the adsorbate in the gas phase (in Pa). A is the surface area of the adsorption site (in m^2). m is the mass of the adsorbate (in kg). and S is the dimensionless sticking coefficient.

The desorption process is the reverse process of adsorption: molecules enter the gas phase from the catalyst surface. In the transition state, there are two degrees of freedom in translation, three degrees of freedom in rotation, and 3N-6 degrees of freedom in vibration. The initial fully adsorbed state contains only vibration degrees of freedom. Therefore, the desorption rate equation:

$$k=\frac{k_b T^3}{h^3}\frac{A(2\pi m k_b)}{\sigma\theta_{rot}}exp(\frac{-E_{des}}{k_b T}) \quad (4)$$

Where, σ is symmetry number. θ_{rot} is the characteristic temperature for rotation. E_{des} is the desorption energy.

For kinetic calculations, the reaction rate of any component M is required, which can be solved using the following differential equation:

$$r_i=\sum_{J=1}^{N}(k_j v_i^j \prod_{k=1}^{M} c_k{}^{v_k{}^j}) \quad (5)$$

Where, k_j is the rate constant of the elementary reaction. v_i is the stoichiometric ratio of component i in the elementary reaction. c_k is the concentration of component k on the catalyst surface.

The speed control step is calculated by the "degree of rate control" (DRC)[1] method, which was introduced by Campbell et al. For primitive step i, the degree of quick control $X_{RC,i}$ is defined as:

$$X_{RC,i}=\frac{k_i}{r}\left(\frac{\partial r}{\partial k_i}\right)_{k_{j=i},K_i}=\left(\frac{\partial \ln r}{\partial \ln k_i}\right)_{k_{j=i},K_i} \quad (6)$$

Where, k_i, K_i, and r are the rate constants, the equilibrium constant, and the reaction rate for step i, respectively.

The elementary reaction of the PDH reaction is as follows:

ST1 $C_3H_8+* \leftrightarrow C_3H_8*$

ST2 $C_3H_8*+* \leftrightarrow C_3H_7*+H_a*$

ST3 $C_3H_7*+* \leftrightarrow C_3H_6*+H_b*$

ST4 $H_a*+H_b* \leftrightarrow H_2*+*$

ST5 $H_2* \leftrightarrow H_2+*$

ST6 $C_3H_6* \leftrightarrow C_3H_6+*$

where * is the active site of the catalyst.

2. Experimental Section

2.1. Catalyst characterization

XRD patterns were obtained by a powder X-ray diffractometer (Ultima IV) using Cu Ka (λ = 0.15406 nm) radiation with a Nickel filter operating at 40 kV and 40 mA in the 2θ range of 20-80° at a scanning rate of 10° min^{-1}. X-ray photoelectron spectra (XPS) were recorded on a Thermo ESCALAB 250Xi. Raman spectra were performed on Renishaw inVia Reflex Raman spectrometer with a 532 nm laser under ambient

conditions. Measurements of UV-Vis diffuse reflectance spectroscopy (UV-Vis DRS) were performed on the UV-Vis spectrophotometer (Hitachi UH4150) with the integration sphere diffuse reflectance attachment. Temperature-programmed reduction with H_2 (H_2-TPR) measurements were performed on micromeritics AutoChem II 2920. 0.05 g samples were pretreated under air atmosphere at 300 °C for 1 h and subsequently cooled to 60 °C. Afterwards, 10% H_2/Ar flow (40 ml min^{-1}) was passed over the catalyst bed while the temperature was ramped from 60 to 700 °C at a heating rate of 10 °C min^{-1}. The hydrogen consumption signal was monitored by a TCD after water removal through cold trap.

2.2. Catalytic tests

The catalytic tests for PDH were performed at 550 °C using a continuous-flow fixed-bed quartz tubular reactor. 0.2 g catalysts and feeds containing 2.5 vol% C_3H_8 in inert gas were used. The C_3H_8 and the reaction products were analyzed by an on-line gas chromatograph (SP-3420) equipped with HP-PLOT/Q (for CH_4, C_2H_4, C_2H_6, C_3H_6 and C_3H_8), TDX-01 (for CO and CO_2) columns as well as flame ionization detector, CO and CO_2 are converted into CH_4 by hydrogenation in a nickel reformer and then detected by a hydrogen flame ionization detector. The propane conversion ($Conv_{C3H8}$), selectivity of products (S_i), yield of products (Y_i), the rate of C_3H_6 formation ($r(C_3H_6)$) were determined from Eqs. (9)–(11), respectively:

$$C_3H_8\ conversion(\%)=((F_{C_3H_8})_{in}-(F_{C_3H_8})_{out})/(F_{C_3H_8})_{in} \quad (7)$$

$$S_i(\%) = (100 n_i (F_i)_{out}) / (3(F_{C_3H_8})_{in} - 3(F_{C_3H_8})_{out}) \quad (8)$$

$$Y_i(\%)=C_{C_3H_8}\cdot S_i/100 \quad (9)$$

$$r(C_3H_6)=(F_{C_3H_8})_{in}Y_i/m_{cat}\cdot 1000/60/42 \quad (10)$$

where i represents the hydrocarbon products in the effluent gas, n_i is the number of carbon atoms of component i, F_i is the corresponding flow rate and m_i is the catalysts mass.

The deactivation constant (h^{-1}) $=[\ln(\frac{1-Con_{Final}}{Con_{Final}}) - \ln(\frac{1-Con_{Initial}}{Con_{Initial}})]/t$, where, the Con_{Final} and $Con_{Initial}$ are the final and initial conversions of the PDH reaction, respectively, and t is the duration of a PDH reaction in hour.

3. Doping formation energy

The formation energy of doped metal to replace Ti lattice is calculated as follows:

$$E(form) = E(Ti_{71}MO_{144}) - (Ti_{72}O_{144}) + \mu(Ti) - \mu(M) \quad (11)$$

Ti-rich condition:

$$\mu(Ti) = \mu(Ti)_{bulk} \quad (12)$$

O-rich condition:

$$\mu(O) = 1/2\mu(O_2) \quad (13)$$

$$\mu(Ti) = E(TiO_2)_{bulk} - 2\mu(O) \quad (14)$$

The formation energy of doped metal to replace O lattice is calculated as follows:

$$E(\,form) = E(Ti_{72}MO_{143}) - (Ti_{72}O_{144}) + \mu(O) - \mu(M) \quad (15)$$

Ti-rich condition:

$$\mu(Ti) = \mu(Ti)_{bulk} \quad (16)$$

$$\mu(O) = 1/2(E(TiO_2)_{bulk} - \mu(Ti)) \quad (17)$$

O-rich condition:

$$\mu(O) = 1/2\mu(O_2) \quad (18)$$

where, $E(Ti_{72}O_{144})$ and $E(Ti_{71}MO_{144})$, $E(Ti_{72}MO_{143})$ are the energy before and after metal M doping. μ(M) is the chemical potential of the metal M taken as the free energy of one M atom in bulk M. $\mu(Ti)_{bulk}$ amounts to the energy of one Ti atom in bulk Ti. $\mu(O_2)$ is the energy of oxygen molecules.

Table S1 Formation energy of metal doping in Ti-rich and O-rich conditions

	Energy / eV	
	Ti-rich condition	**O-rich condition**
Sc-Ti	-2.52	-7.67
Ti-Sc	-1.04	-6.19
Sc replaces O_{2c}	2.07	4.65
V-Ti	-1.61	-6.76
Ti-V	1.16	-3.99
V replaces O_{2c}	4.30	6.88

Cr-Ti	2.33	-2.82
Ti-Cr	2.98	-2.17
Cr replaces O_{2c}	4.78	7.36
Mn-Ti	1.98	-3.17
Mn replaces O_{2c}	3.65	6.23

4. Effective Bader charge of intact and defective surface atoms

Table S2 Bader charge of two coordinated oxygen and four coordinated metal atoms on perfect TiO_2(101) surfaces (M: Five coordination metal atoms on the surface, as shown in Ti_{5c} in Figure 1. O: two-coordinated oxygen atoms on the surface, as shown in O_{2c} in Figure 1)

	M			O		
TiO_2	2.026	2.025	2.026	-0.922	-0.922[c]	-0.925
Sc-Ti	2.028	2.005[a]	2.025	-0.926	-0.989[c]	-0.923
V-Ti	2.019	1.862[a]	2.023	-0.923	-0.833[c]	-0.923
Cr-Ti	2.028	1.772[a]	2.026	-0.924	-0.814[c]	-0.924
Mn-Ti	2.017	1.713[a]	2.024	-0.912	-0.831[c]	-0.918
Ti-Sc	2.029	2.002[b]	2.026	-0.920	-0.980[c]	-0.921
Ti-V	2.023	2.029[b]	2.022	-0.929	-0.872[c]	-0.931
Ti-Cr	2.018	2.032[b]	2.020	-0.916	-0.851[c]	-0.928

[a] bader charge value of doped metal atoms

[b] bader charge value of Ti atoms

[c] bader charge value of oxygen atoms connected to doped metals

Table S3 Bader charge of two coordinated oxygen and four coordinated metal atoms on defective TiO_2(101) surfaces (M: The left and right are the five coordinated Ti atoms on the surface, and the middle are metal atoms connected by oxygen vacancies. O: Two coordinated oxygen atoms connected by oxygen vacancies)

	M			O		
TiO_2	2.019	1.890	2.013	-0.947	-	-0.946
Sc-Ti	2.024	1.960[a]	2.019	-0.957	-	-0.960
V-Ti	2.015	1.794[a]	2.014	-0.953	-	-0.944
Cr-Ti	2.014	1.671[a]	2.007	-0.948	-	-0.951
Mn-Ti	2.007	1.416[a]	2.003	-0.936	-	-0.947
Ti-Sc	2.015	1.812[b]	2.014	-0.945	-	-0.948
Ti-V	2.018	1.893[b]	2.019	-0.952	-	-0.955
Ti-Cr	2.022	1.783[b]	2.026	-0.932	-	-0.934

[a] bader charge value of doped metal atoms

[b] bader charge value of Ti atoms

5. d-band center of the doping metal and Ti atom of TiO_2(101)

Table S4 d-band center of the doping metal and Ti atom of TiO_2(101)

	d band center / eV
TiO_2	-1.04
Sc-Ti	-1.04
V-Ti	-1.24
Cr-Ti	-1.01
Mn-Ti	-0.65
Ti-Sc	-1.02
Ti-V	-1.24
Ti-Cr	-1.00

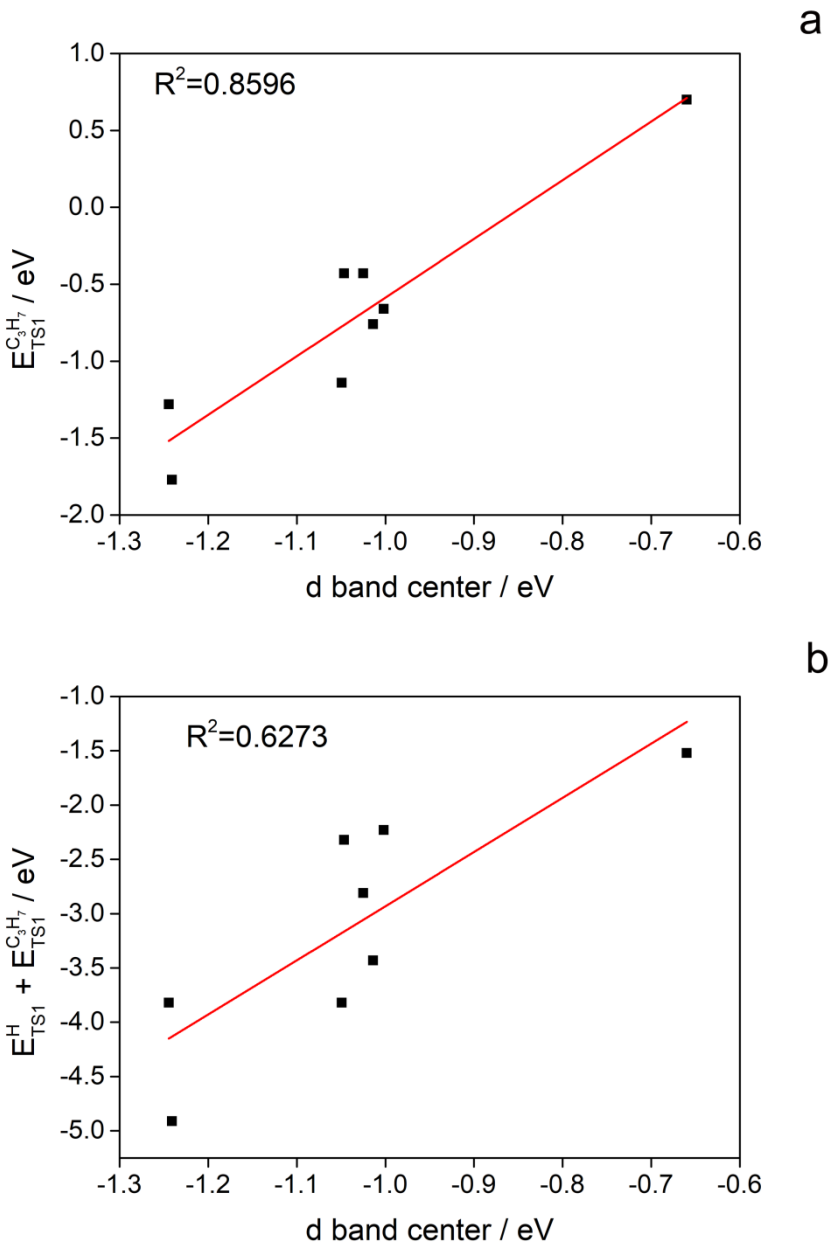

Figure S1. Correlation between the d band center and (left) the binding energies of C_3H_7 in TS1 configurations, (right) sum of binding energies of C_3H_7 and H in TS1 configuration.

6. Dehydrogenation transition state structure

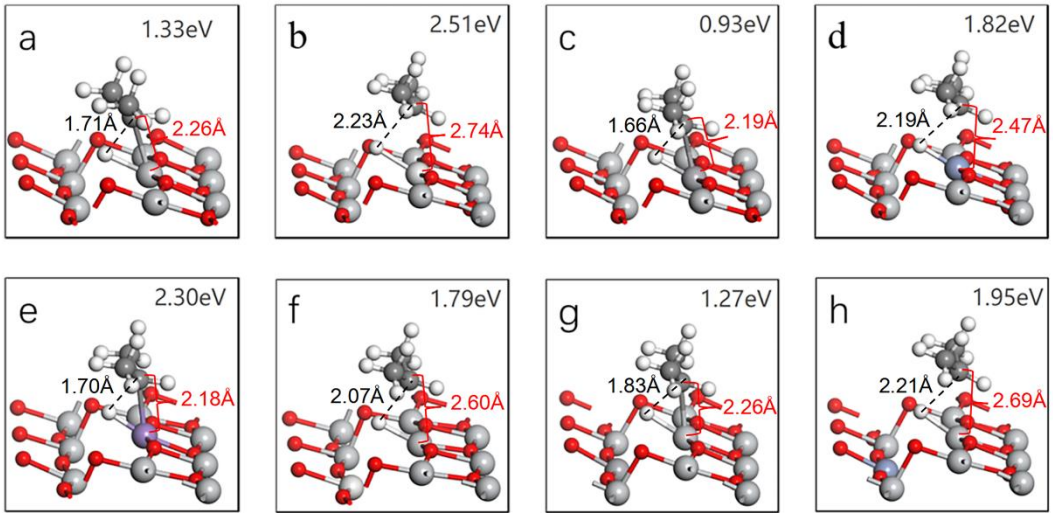

Figure S2. First step dehydrogenation transition state structure and energy barrier: a) TiO_2, b) Sc-Ti, c) V-Ti, d) Cr-Ti, e) Mn-Ti, f) Ti-Sc, g) Ti-V, h) Ti-Cr.

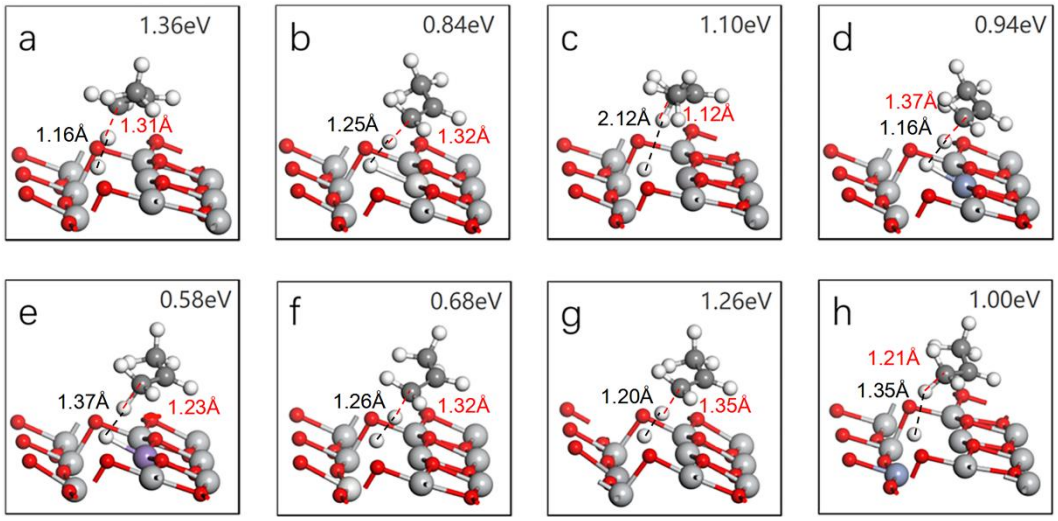

Figure S3. Second step dehydrogenation transition state structure and energy barrier: a) TiO_2, b) Sc-Ti, c) V-Ti, d) Cr-Ti, e) Mn-Ti, f) Ti-Sc, g) Ti-V, h) Ti-Cr.

7. Energy barrier decomposition calculation

To provide further insight into the C_3H_8 dissociation energy barriers, we use the following scheme to decompose the calculated barrier E_{a1} and E_{a2}. E_{a1} and E_{a2} of the different catalysts' surfaces, shown as calculated in Eqs. (19) and (20)[2]:

$$E_{a1}=\Delta E_{slab}+\Delta E_{def\text{-}C_3H_8}-E_{IS1}^{C_3H_8}+E_{TS1}^{C_3H_7}+E_{TS1}^{H}-E_{int\text{-}C_3H_7\cdots H} \quad (19)$$

$$E_{a2}=\Delta E_{slab}+\Delta E_{def\text{-}C_3H_7\&H}-E_{IS2}^{C_3H_7\&H}+E_{TS2}^{C_3H_6}+E_{TS1}^{H_2}-E_{int\text{-}C_3H_6\cdots H\cdots H} \quad (20)$$

Where ΔE_{slab} is the influence of the structural change of the catalysts substrate from IS to TS on the barrier (due to the vacancy of the O atom and Transition metal doping). $\Delta E_{def\text{-}C3H8}$ and $\Delta E_{def\text{-}C3H7\&H}$ are called deformation energy, which reflects the effect of the structural deformation of C_3H_8 and C_3H_7&H on the activation energy. $E_{IS1}^{C_3H_8}$ and $E_{IS2}^{C_3H_7\&H}$ are the adsorption energies of C_3H_8 and C_3H_7&H in the IS configuration. $E_{TS1}^{C_3H_7}$, E_{TS1}^{H}, $E_{TS2}^{C_3H_6}$, $E_{TS2}^{H_2}$ are the binding energies of C_3H_7 (without H), H (without C_3H_7) in TS1 configurations, and C_3H_6 (without H_2), H_2 (without C_3H_6) in TS2 configurations, respectively. $E_{int\text{-}C_3H_7\cdots H}$ and $E_{int\text{-}C_3H_6\cdots H\cdots H}$ are the interaction energy between H and C_3H_7 in TS1, H_2 and C_3H_6 in TS2. The contributions to the energy barrier E_{a1} and E_{a2} of each term are displayed in Table S4 and S5, respectively.

Table S5 The parts of the energy decomposition of the calculated dissociation energy barrier. Reaction : $C_3H_{8ads} \rightarrow C_3H_{7ads} + H_{ads}$ (The value in parentheses is the difference from pure TiO_2)

	ΔE_{slab}	$\Delta E_{def-C_3H_8}$	$E_{IS1}^{C_3H_8}$	$E_{TS1}^{C_3H_7}$	E_{TS1}^{H}	$E_{int-C_3H_7\cdots H}$	E_{a1}
TiO_2	0.35	2.32	-0.21	-1.14	-2.68	-2.27	1.33
Sc-Ti	0.39	4.77	-0.17	-0.43	-1.89	0.5	2.51
	(0.04)	(2.45)	(0.04)	(0.71)	(0.79)	(2.77)	
V-Ti	0.97	2.1	0.03	-1.77	-3.14	-2.8	0.93
	(0.62)	(-0.22)	(0.24)	(-0.63)	(-0.46)	(-0.53)	

Cr-Ti	-0.16	4.76	-0.13	-0.76	-2.67	-0.52	1.82
	(-0.51)	(2.44)	(0.08)	(0.38)	(0.01)	(1.75)	
Mn-Ti	0.25	2.32	-0.08	0.7	-2.22	-1.17	2.3
	(-0.1)	(0)	(0.13)	(1.68)	(0.46)	(1.1)	
Ti-Sc	0.31	4.97	-0.06	-0.43	-2.38	0.74	1.79
	(-0.04)	(2.65)	(0.15)	(0.71)	(0.3)	(3.01)	
Ti-V	0.67	2.73	0.16	-1.28	-2.54	-1.85	1.27
	(0.32)	(0.4)	(0.37)	(-0.14)	(0.14)	(0.42)	
Ti-Cr	0.68	4.77	-0.06	-0.66	-1.57	1.33	1.95
	(0.33)	(2.45)	(0.15)	(0.48)	(1.11)	(3.6)	

Table S6 The parts of the energy decomposition of the calculated dissociation energy barrier. Reaction : $C_3H_{7ads} + H_{ads} \rightarrow C_3H_{6ads} + H_{2ads}$ (The value in parentheses is the difference from pure TiO_2)

	ΔE_{slab}	$\Delta E_{def-C_3H_7\&H}$	$E_{IS2}^{C_3H_7\&H}$	$E_{TS2}^{C_3H_6}$	$E_{TS2}^{H_2}$	$E_{int-C_3H_6\cdots H\cdots H}$	E_{a2}
TiO_2	-0.35	-1.48	-3.55	-0.31	3.31	3.36	1.36
Sc-Ti	-0.19	-0.74	-2.77	0	1.14	2.14	0.84
	(0.16)	(0.74)	(0.78)	(0.31)	(-2.17)	(-1.22)	
V-Ti	-0.15	-0.69	-3.55	1.1	1.44	4.15	1.1
	(0.2)	(0.79)	(0)	(1.41)	(-1.87)	(0.79)	
Cr-Ti	-1.51	-1.05	-2.97	-0.08	0.94	0.33	0.94

	(-1.16)	(0.43)	(0.59)	(0.23)	(-2.37)	(-3.03)	
Mn-Ti	-0.26	0.17	-2.4	2.7	2.63	7.06	0.58
	(0.09)	(1.65)	(1.15)	(3.01)	(-0.68)	(3.7)	
Ti-Sc	-0.29	-0.85	-2.84	-0.09	0.76	1.69	0.68
	(0.06)	(0.63)	(0.71)	(0.22)	(-2.55)	(-1.67)	
Ti-V	0.63	-1.32	-3.42	-1.32	-0.91	-0.76	1.26
	(0.98)	(0.16)	(0.13)	(-1.01)	(-4.22)	(-4.12)	
Ti-Cr	-1.43	0.37	-2.87	0.07	3.15	4.03	1
	(-1.08)	(1.85)	(0.68)	(0.38)	(-0.16)	(0.67)	

8. Different reaction paths for the first step dehydrogenation

Taking V-Ti catalyst and Cr-Ti catalyst as examples, the energy barriers of different binding sites of H during the first dehydrogenation are calculated. The energy barrier and final state structure of the reaction are shown in Figure S4. It can be clearly seen from the figure that the energy barrier of the reaction path where H is located at the oxygen vacancy is much lower than the reaction path where hydrogen is combined with O_{2c}. This is because when oxygen is removed to form oxygen vacancies, a negative charge band is formed at the oxygen vacancies, which will greatly reduce the energy when adsorbing H. At the same time, H is located at the oxygen vacancy and does not form steric hindrance.

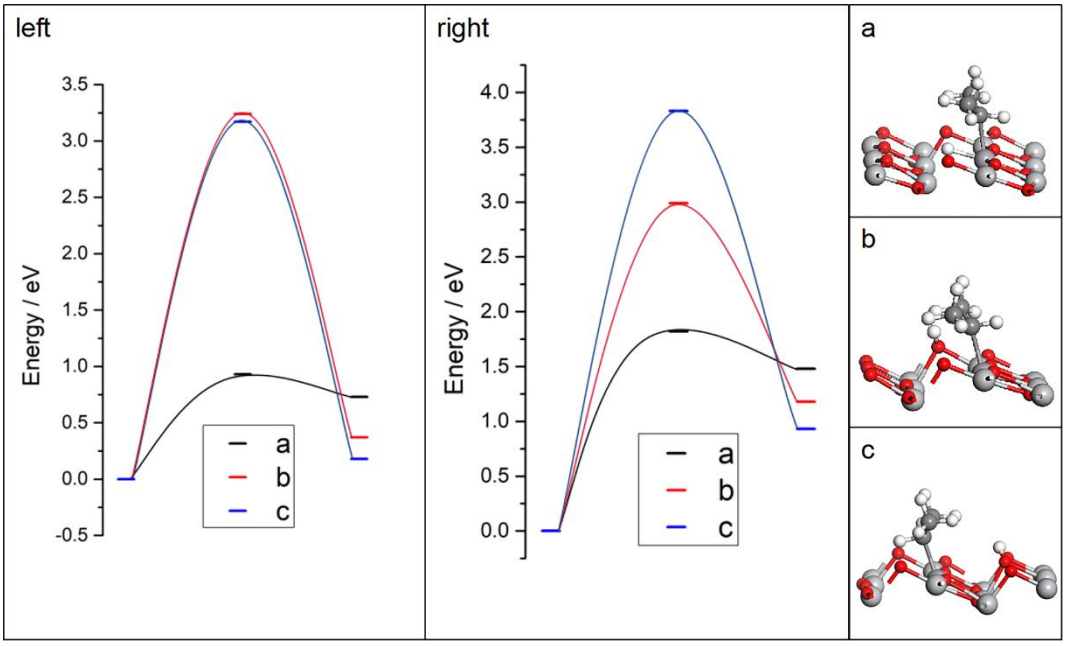

Figure S4. the energy barrier for the first dehydrogenation of left)V-Ti and right)Cr-Ti. Structure diagram of dehydrogenation transition state of a)H is at the oxygen vacancy, b)H is located on the oxygen vacancy adjacent to O_{2c} and c)H is located on O_{2c} not adjacent to the

oxygen vacancy.

9. H transfer barrier and second step dehydrogenation barrier

Table S7 shows the energy barrier for H transfer to the nearest O_{2C} and the energy barrier for the second step dehydrogenation. Because of the strong attraction of the negative charge band at the oxygen vacancy to H, the transfer of H from the oxygen vacancy to the nearest O_{2c} requires higher energy. The energy for further dehydrogenation is much lower than the energy transferred by H. Therefore, the H produced by the first dehydrogenation is located at the oxygen vacancy, and the second dehydrogenation is directly carried out to form hydrogen and propylene without H transfer.

Table S7 H transfer barrier and second step dehydrogenation barrier(eV)

	H transfer	**Second step dehydrogenation**
Sc-Ti	2.17	0.84
V-Ti	1.90	1.10
Cr-Ti	2.01	0.94
Mn-Ti	1.81	0.58
Ti-Sc	1.86	0.68
Ti-V	1.85	1.26
Ti-Cr	1.78	1.00

10. Microscopic dynamic analysis

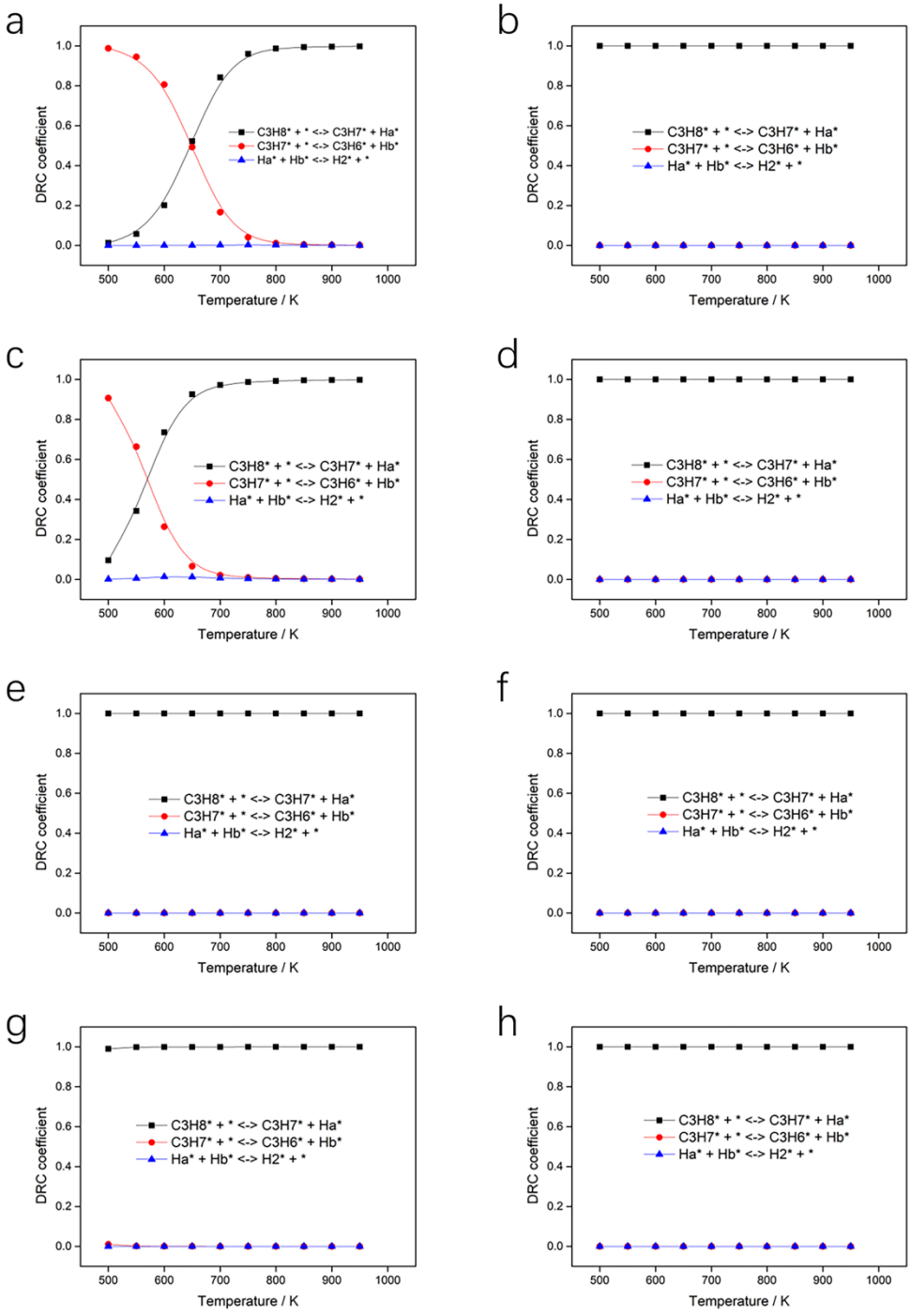

Fig. S5. The degree of rate control as a function of temperature for a) TiO_2, b) Sc-Ti, c) V-Ti, d) Cr-Ti, e) Mn-Ti, f) Ti-Sc, g) Ti-V, h) Ti-Cr.

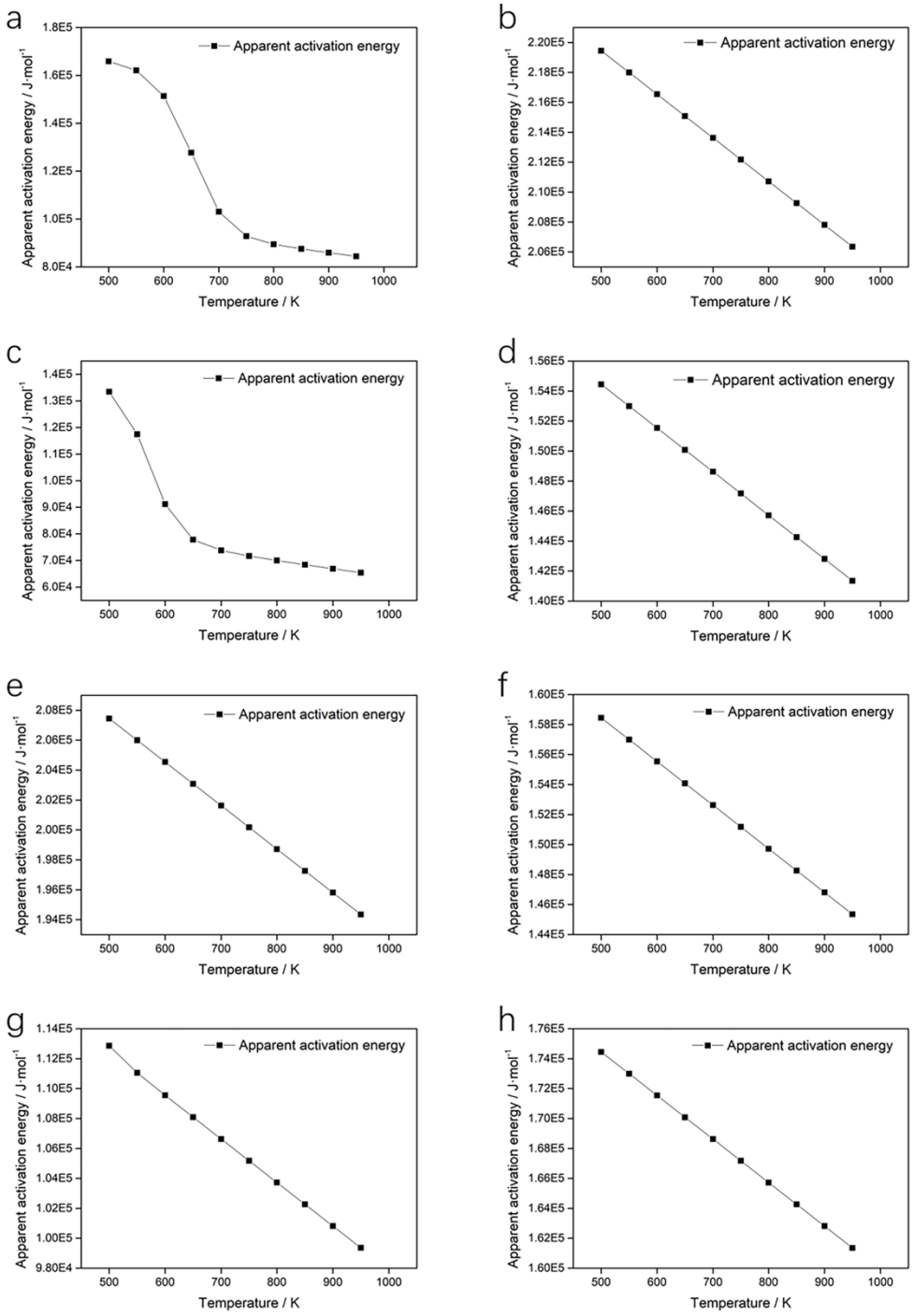

Fig. S6. Apparent activation energy as a function of temperature for a) TiO_2, b) Sc-Ti, c) V-Ti, d) Cr-Ti, e) Mn-Ti, f) Ti-Sc, g) Ti-V, h) Ti-Cr.

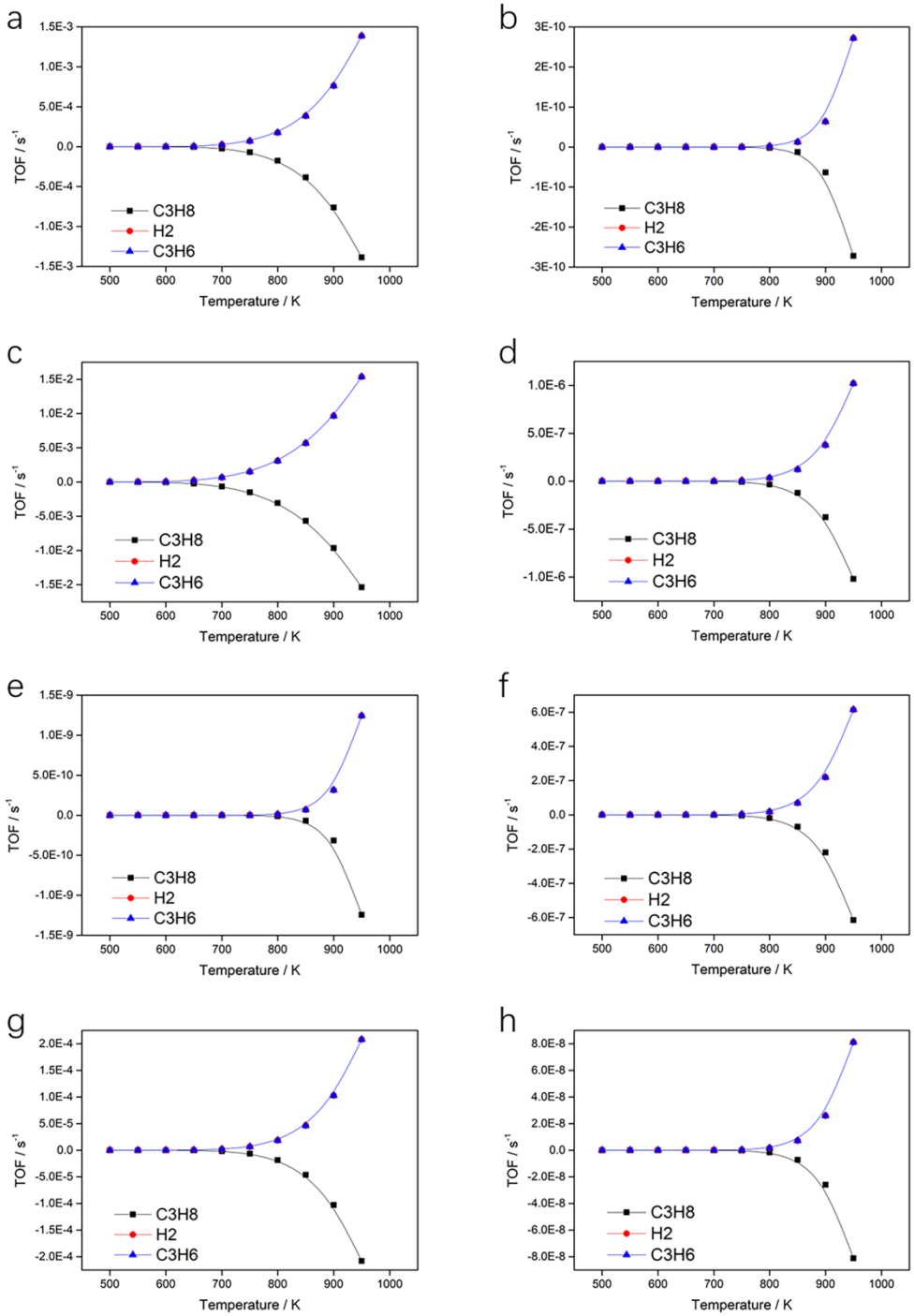

Fig. S7. Rate of C_3H_8, H_2, and C_3H_6 as a function of temperature for a) TiO_2, b) Sc-Ti, c) V-Ti, d) Cr-Ti, e) Mn-Ti, f) Ti-Sc, g) Ti-V, h) Ti-Cr.

11. Raman spectra, V 2p2/3 XPS spectra and UV-Vis absorption spectra

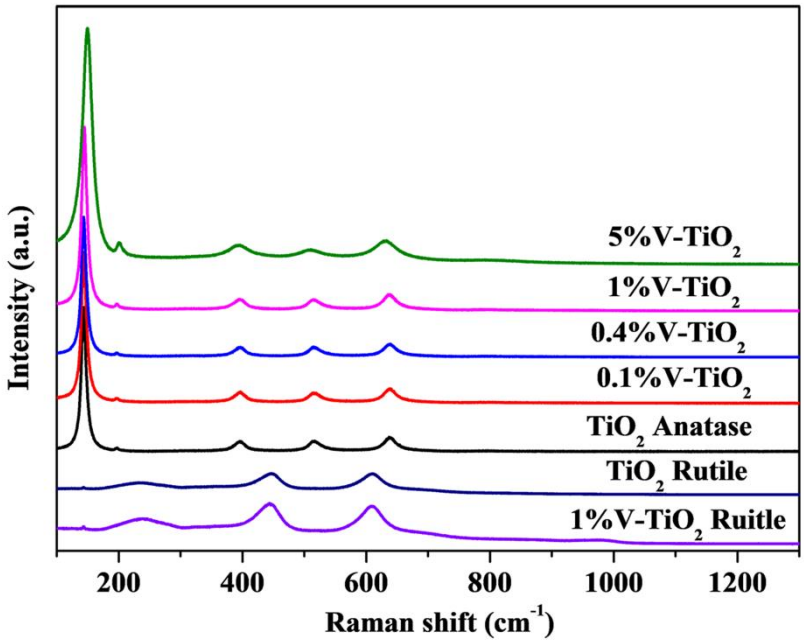

Fig. S8. Raman spectra of the x%V-TiO_2, 1%V-TiO_2 Rutile, pure TiO_2 (anatase and rutile phase) and V_2O_5.

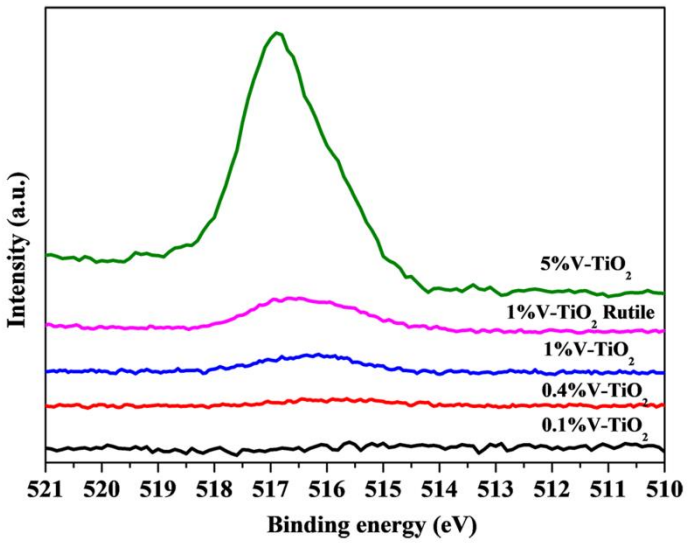

Fig. S9. V 2p2/3 XPS spectra of the the x%V-TiO_2 and 1%V-TiO_2 Rutile catalysts.

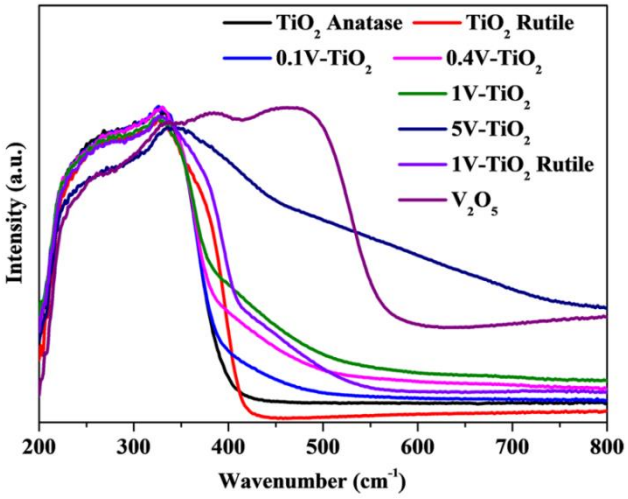

Fig. S10. UV-Vis absorption spectra of the x%V-TiO_2, 1%V-TiO_2 Rutile, pure TiO_2(anatase and rutile phase) and V_2O_5.

12. Catalyst performance of various catalysts

Table S8. Catalytic performance of various catalysts from literature and from the present study in the non-oxidative propane dehydrogenation to propene

Catalyst	m/g	T/°C	C(C_3H_8)	S(C_3H_6)	F_{total}/mL·min^{-1}	Feeding gas composition	WHSV / h^{-1}	STY(C_3H_6)/ kg·h^{-1}·kg^{-1}	Ref.
ZrO_2(reduced in CO)	0.07	550	28.4	87.0	10	40 vol% C_3H_8 in N_2	6.7	1.58	3
$PtZn_4$@S-1-H	0.3	550	47.4	93.2	40	25 vol% C_3H_8 in N_2	3.6	1.59	4
Cr_2O_3/ZrO_2	0.2	550	60.9	76.2	20	2.5 vol% C_3H_8 in N_2	0.3	0.13	5
Cr5/SBA-1	0.2	550	33.0	86.0	30	C_3H_8/He/N_2=5:1:9	1.2	0.32	6
Ga_2O_3/Al_2O_3	0.2	600	33.4	92.0	20	2.5 vol% C_3H_8 in N_2	0.3	0.09	7
Sn-HMS	1.5	600	40.0	90.0	5	Pure C_3H_8	0.39	0.14	8
5-10nm TiO_2	0.3	550	11	98	12	C_3H_8/N_2=1:2	1.56	0.17	9
5-10nm TiO_2	0.3	600	31	91	12	C_3H_8/N_2=1:2	1.56	0.44	9
1%V-TiO_2	0.3	550	12.5	98	12	C_3H_8/N_2=1:2	1.56	0.18	This work

Reference

[1] M. Coltheart, K. Rastle, C. Perry, R. Langdon, J. Ziegler, DRC: A dual route cascaded model of visual word recognition and reading aloud, Psychological Review, 108 (2001) 204-256.

[2] X. Wen, P. Bai, Z. Han, S. Zheng, B. Luo, T. Fang, W. Song, Effect of vacancy on adsorption/dissociation and diffusion of H_2S on Fe(100) surfaces: A density functional theory study, Appl. Surf. Sci. 2019, 465, 833-845.

[3] Zhang, Y.; Zhao, Y.; Otroshchenko, T.; Lund, H.; Pohl, M.; Rodemerck, U.; Linke, D.; Jiao, H.; Jiang, G.; Kondratenko, E.V. Control of coordinatively unsaturated Zr sites in ZrO2 for efficient C-H bond activation. Nat. Commun. 2018, 9, 3794-3804.

[4] Sun, Q.; Wang, N.; Fan, Q.; Zeng, L.; Mayoral, A.; Miao, S.; Yang, R.; Jiang, Z.; Zhou, W.; Zhang, J.; Zhang, T.; Xu, J.; Zhang, P.; Cheng, J.; Yang, D.-C.; Jia, R.; Li, L.; Zhang, Q.;Wang, Y.; Terasaki, O.; Yu, J. Subnanometer Bimetallic Pt-Zn Clusters in Zeolites for Propane Dehydrogenation. Angew. Chem. Int. Ed. 2020, 59, 19450-19459.

[5] Zhang, X.; Yue, Y.; Gao, Z. Chromium Oxide Supported on Mesoporous SBA-15 as Propane Dehydrogenation and Oxidative Dehydrogenation Catalysts. Catal. Lett. 2002, 83, 19-25.

[6] Michorczyk, P.; Pietrzyk, P.; Ogonowski, J. Preparation and Characterization of SBA-1 Supported Chromium Oxide Catalysts for CO_2 Assisted Dehydrogenation of Propane. Microporous Mesoporous Mater. 2012, 161, 56-66.

[7] Xu, B.; Zheng, B.; Hua, W.; Yue, Y.; Gao, Z., Support Effect in Dehydrogenation of Propane in the Presence of CO_2 over Supported Gallium Oxide Catalysts. J. Catal. 2006, 239, 470-477.

[8] Wang, G.; Zhang, H.; Zhu, Q.; Zhu, X.; Li, X.; Wang, H.; Li, C.; Shan, H., Sn-containing Hexagonal Mesoporous Silica (HMS) for Catalytic Dehydrogenation of Propane: An Efficient Strategy to Enhance Stability. J. Catal.

2017, 351, 90-94.

[9] Xie, Z.; Yu, T.; Song, W.; Li, J.; Zhao, Z.; Liu, B.; Gao, Z.; Li, D. Highly Active Nanosized Anatase TiO_{2-x} Oxide Catalysts In Situ Formed through Reduction and Ostwald Ripening Processes for Propane Dehydrogenation. ACS Catal. 2020, 10, 14678-14693.